Surface modification of binder-jet additive manufactured Inconel 625 via electrospark deposition

Pablo D. Enrique[a],[*], Ehsan Marzbanrad[a], Yahya Mahmoodkhani[a], Zhen Jiao[b], Ehsan Toyserkani[a], Norman Y. Zhou[a]

[a] University of Waterloo, 200 University Ave W, Waterloo, Ontario N2L 3G1, Canada
[b] Huys Industries Ltd., 175 Toryork Drive, Unit 35 Weston, Ontario M9L 1X9, Canada

ABSTRACT

Advancements in additive manufacturing have facilitated its adoption in the aerospace industry, where a lower production volume for high-valued components is required. However, the poor surface quality of additively manufactured parts is detrimental to component lifespan and requires additional post-processing steps. Here, we address surface roughness and near-surface porosities in binder-jet additively manufactured Inconel 625 parts using an electrospark deposition (ESD) technique. Localized surface melting and material transfer from the ESD electrode results in a near-surface region with increased density (from 62.9% to 99.2%) and increased hardness (from 109 HV to 962 HV). The use of an AA4043 aluminum alloy electrode forms a nickel aluminide inter-metallic coating when deposited on Inconel 625, with the potential for use in applications that require resistance to high temperature oxidation.

1. Introduction

Additive manufacturing allows for faster and more cost-effective low-volume manufacturing of components and replacement parts in the aerospace industry for a wide range of materials [1–5], where the parts have bulk properties comparable to those made by traditional manu-facturing processes but they suffer from greater near-surface porosity and surface roughness. This has been reported to negatively influence the mechanical properties of additively manufactured parts [6–8], providing an incentive for the use of a post-processing step that ad-dresses surface finish. This is especially true in binder-jet additive manufacturing (BJAM), which can suffer from density variations as a result of porous regions that develop near the surface [9]. Particles in the near-surface region exhibit some necking but do not show extensive coalescence like particles within the bulk. One potential cause identi-fied in literature for this near-surface porosity is binder oversaturation, which results in infiltration beyond the desired part boundary [10]. If more than the equilibrium amount of binder is used, binder will spread to unsaturated areas due to capillary and surface tension forces. This forms a porous region at the surface, where the branching binder does not adequately hold the powder particles together and results in lower coordination number and poor sintering [11].

The typical CNC (computer numerical control) surface machining

step used to remove surface defects faces several drawbacks; as a sub-tractive technique, it requires that parts are created larger than their desired final geometry. The resulting longer printing times, as well as loss of material, geometric limitations of CNC machining, and low machinability of superalloy materials encourage the implementation of alternate surface finishing processes. Electrospark deposition (ESD) is a pulsed-arc deposition technique often used for surface modification of conductive substrates, including the application of wear and corrosion resistant coatings [12,13]. ESD has the potential to achieve good sur-face finish [14,15], reduce porosity, and alloy the component surface for use in specific applications. Here, we demonstrate the application of an ESD process using an AA4043 aluminum alloy electrode to modify the surface of a BJAM Inconel 625 substrate. Good surface conditions were achieved by optimizing energy input during the ESD process, with increasing energy input resulting in decreasing near-surface porosity. The resulting coating not only reduced near-surface porosity below 1% and increased surface hardness by up to 900%, it also formed a nickel aluminide intermetallic coating with potential use in applications that require high temperature oxidation resistance.

---

* Corresponding author.
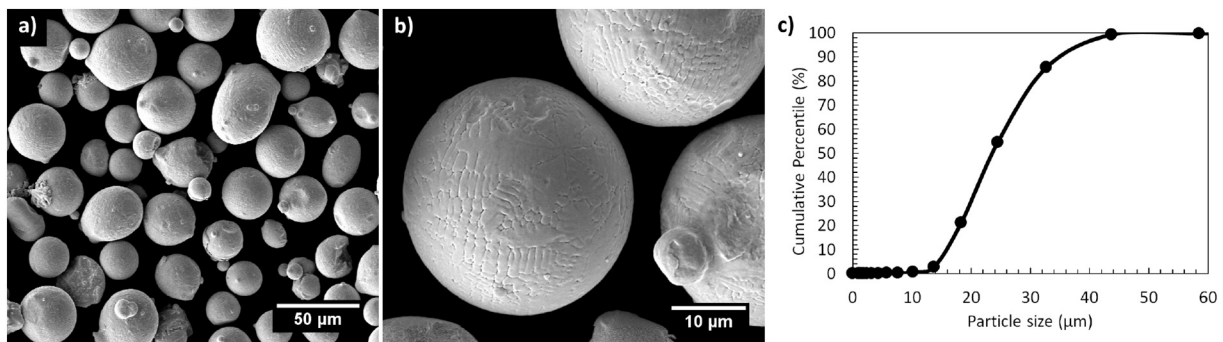 E-mail address: pdenriqu@uwaterloo.ca (P.D. Enrique).

Fig. 1. a, b) SEM images of Inconel 625 powder particles and c) the cumulative particle size distribution.

2. Materials and methods

2.1. Binder jet printing process

An Inconel 625 powder batch with an average particle size of approximately 24 μm was used in the BJAM process. Fig. 1a and b show the mostly spherical shape of the powder particles, and Fig. 1c shows the particle size distribution. The nominal and measured composition of Inconel 625 is listed in Table I.

The printing process was performed as described elsewhere [16]. A summary however follows. A 3D SYSTEMS ZCorp Z 510/310 binder-jet powder-bed system and 20 mm by 10 mm by 2.5 mm rectangular CAD model was used. A 70 μm layer height, zb60 binder, 360 dpi resolution, 100% core and 200% shell saturation, and 35 °C 3-hour post-printing hold temperature was used. Printed samples were coated with zb60 binder and 3-wt% polyvinyl acetate (PVA) to add strength, and then dried with a 100 W tungsten lamp.

2.2. Sintering process

The as-printed parts were subjected to a sintering process in a high purity argon environment with 250 Pa of positive pressure for joining of the powder particles. The heating profile involved an initial 3 °C/min ramp-up to 527 °C under a 5% hydrogen (argon balance) atmosphere and a hold period of 3 h, during which the binder burn-off occurred. Then the atmosphere was switched to high purity argon and a ramp rate of 5 °C/min was used to reach 1200 °C. A holding period of 5 h was used for sintering the parts. At the end of the holding period, the parts were removed from the furnace and water quenched.

2.3. ESD processing and materials

Deposition of AA4043 was performed using a Huys Industries ESD machine with a manual applicator. ESD works by repeated discharging of a capacitor at high frequency through a consumable electrode onto a conductive substrate. This results in short duration pulses of high current, such that a very small amount of molten material transfers with each pulse. A total coating time of 40 s on a 0.5 cm^2 area was kept constant for each set of parameters tested. The chosen capacitance and voltage values are shown in Table II, with frequency kept constant. Input energy (E) with each deposition pulse is calculated using the energy of a capacitor,

Table II
ESD coating process parameters.

Label	Capacitance	Voltage	Frequency	Energy
Low	80 μF	100 V	170 Hz	400 mJ
Medium	120 μF	100 V	170 Hz	600 mJ
High	120 μF	130 V	170 Hz	1014 mJ

$$E = \frac{1}{2}CV^2 \tag{1}$$

where C is the capacitance and V is the voltage. Therefore, only the capacitance and voltage are considered when optimizing ESD parameters in this study, although frequency can also have some effect on the deposited material. A visual example of these coatings is shown in Fig. 2.

All depositions were performed manually with the use of an argon cover gas (at 10 L/min) and a bidirectional raster scan pattern was used to cover the surface. The AA4043 electrode used for ESD coating was 2.1 mm in diameter and the composition was determined by EDX to be 94% Al and 6% Si, which is close to the nominal AA4043 composition (94.8% Al and 5.2% Si).

2.4. Characterization methods

Analysis was performed with a Zeiss UltraPlus scanning electron microscope (SEM) with an energy-dispersive X-ray spectroscopy (EDX) attachment capable of area mapping. All SEM images are obtained with a 20 kV accelerating voltage and 60 μm aperture. Grazing incidence X-ray diffraction (GIXRD) analysis was performed using a PANalytical X'Pert Pro MRD HR-XRD, with Cu-K(alpha) radiation, a scanning range from 20 to 100°, a scan step size of 0.1° and a 5 s step time. Peaks are matched with the use of PANalytical X'Pert HighScore Plus software. Optical images were obtained with the use of an Oxford BX51M optical microscope (OM) and porosity measurements were made using ImageJ threshold analysis on cross sections of the samples. Surface roughness measurements of 2 mm by 2.5 mm areas were performed with a Keyence laser scanning confocal microscope and waveform correction during post-processing of results. Microhardness measurements were obtained using a Wolpert Wilson 402 MVD micro Vickers hardness tester (100 gf and 15 s dwell time) on cross sectioned samples of the ESD electrode and additive manufactured substrate.

Table I
Nominal and EDX measured composition (wt%) of major alloying elements in Inconel 625.

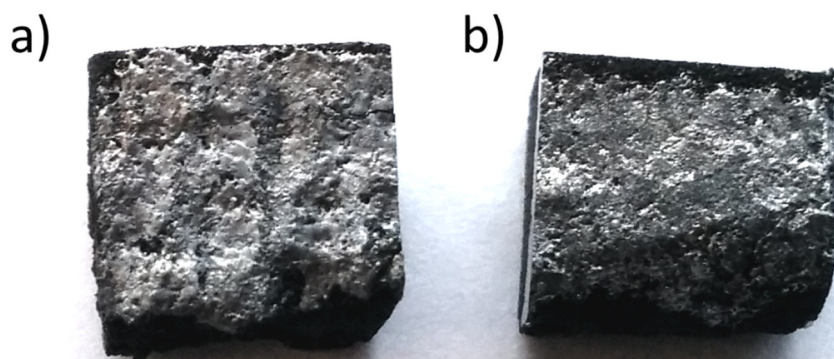| Label	Cr	Mo	Nb	Fe	Al	Si	Ti	C	Ni
Nominal	20.0–23.0	8.0–10.0	3.15–4.15	5.0	0.4	0.5	0.4	≤0.1	58.0-bal.
EDX	20.5	10.3	3.7	4.8	0.9	0.7	0.7		58.4

Fig. 2. BJAM Inconel 625 part with ESD coatings deposited using a) medium and b) low energy parameters.

3. Results and discussion

3.1. Analysis of As-sintered BJAM part

As-sintered BJAM parts display a dense inner region (Fig. 3a) and highly interconnected pores near the surface (Fig. 3b). These regions are characterized by their higher (92.8 ± 0.8%) and lower (62.9 ± 3.0%) density, respectively. The outermost powder particles in Fig. 3b appears brighter due to poor connection with the bulk of the sample, resulting in charge accumulation when the sample interacts with the electron beam during scanning electron microscope (SEM) imaging. It is expected that a combination of factors contribute to this porous structure: binder spreading during printing, higher binder saturation in the shell, and binder degassing through the surface of the part during sintering can lead to particle separation and low density. However, the bulk density is higher when compared to other BJAM Inconel 625 samples in the literature that were sintered at the same temperature [17], attributed to a smaller particle size and a longer sintering time. The particle sintering kinetics are directly affected by the available surface energy, which acts as a driving force during sintering. The greater surface area per unit volume provided by smaller particles results in a higher surface energy and a faster sintering process [18].

SEM analysis indicates the presence of two different types of segregation within the final sintered part. Intraparticle segregation appears dark under inverted backscatter imaging (Fig. 4b) – which in this case is indicative of larger atomic number – while interparticle segregation appears white or gray, indicating the presence of lighter elements in higher quantities. Intraparticle segregation is Nb and Mo-rich (indicated in Table III and Fig. 4c by arrow 1) and is differentiated by its distinct lack of oxygen. One possible candidate for this phase of Inconel 625 is NbC with Mo substitution. Carbides commonly form in Inconel 625 after solidification [19,20], aging and annealing [21,22], and sintering of BJAM Inconel 625 [17]. A Time-Temperature-Transformation (TTT) diagram of solution annealed Inconel 625 indicates that a NbC phase can be expected to form under 1 h at temperatures between 800 and 1000 °C, and finely dispersed carbides have been reported to form after exposure on the order of 10 min at these temperatures [23]. This carbide formation mechanism is suggested because of the slow ramp-up rate (5 °C/min) used during sintering, and the very fast cooling rate from water quenching after sintering. The lack of a reliable carbon EDX peak is expected for this characterization technique, while the detection of Ni, Cr and Fe when measuring this carbide can be explained by considering the small precipitate size and larger interaction volume of EDX. Instead, XRD analysis was used to confirm the presence of a NbC phase (Fig. 5).

Interparticle segregation exhibits a strong oxygen peak during EDX analysis, as well as Cr-rich and (Nb, Mo)-rich regions. As Fig. 4b shows, there are two interparticle phases present; the bright white phase indicates lower atomic number while the gray phase is composed of some heavier elements. Their respective compositions are listed in Table III, and one oxide phase could be clearly identified using XRD (Cr_2O_3). Identification of other oxide phases is limited by small volume fractions, background radiation, peak overlap, and peak matching
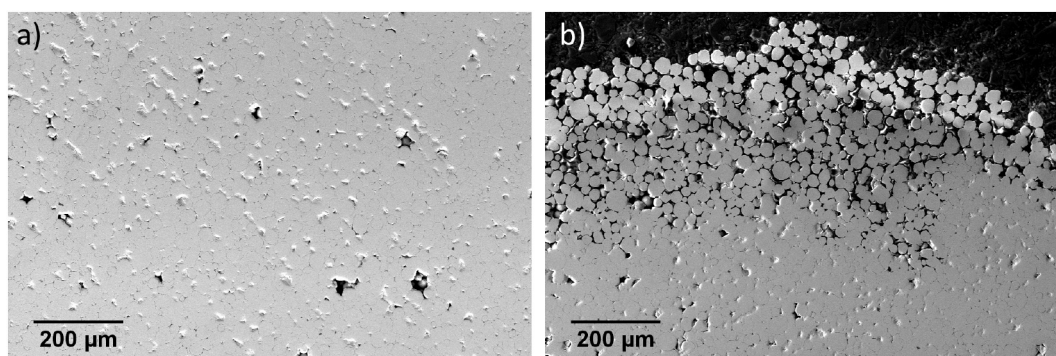

Fig. 3. SEM image of cross-sectioned BJAM part after sintering a) within the bulk and b) near the surface.
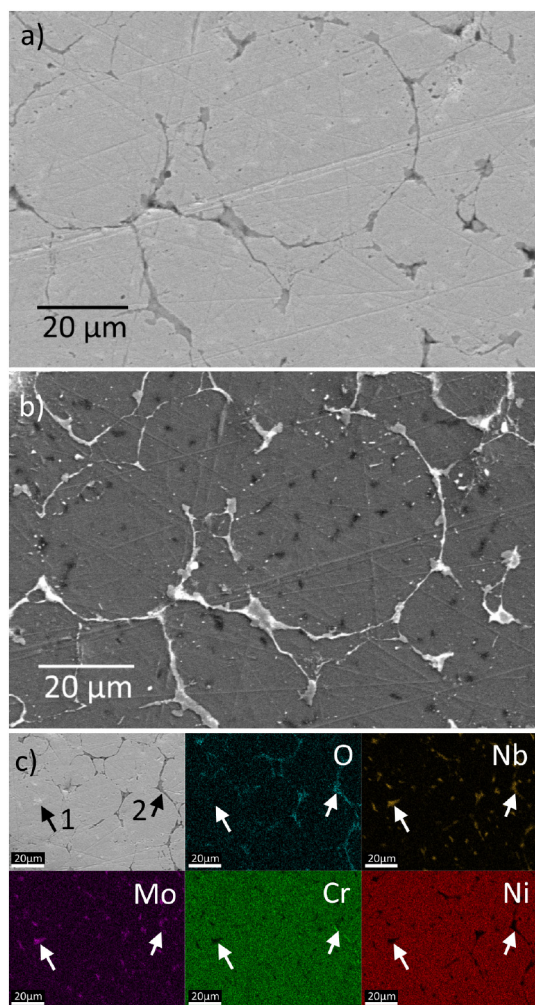
Fig. 4. SEM of cross-sectioned Inconel 625 BJAM part after sintering using a) secondary electron imaging, b) backscatter electron imaging with inverted polarity (darker shade represents increasing atomic number), and c) EDX map with two phases of interest labelled 1 and 2.

Table III
EDX composition (wt%) in intra- and interparticle segregation.

Location	Nb	Mo	Cr	Ni	O	Fe	Ti	Al	Si
Intraparticle (Nb-rich)	48.2	9.9	11.3	26.0		2.5	2.2		
Interparticle (Cr-rich)	6.1	1.6	59.7	11.5	16.3	2.2	1.0	1.2	0.6
Interparticle (Nb-rich)	33.2	3.6	16.1	20.8	21.3	2.5	2.5	0.1	

uncertainties. Since these oxide phases appear within the sintered part, they cannot be attributed to oxide formation when samples are removed from the furnace after sintering. Formation of Cr oxides have been shown to preferentially occur in Inconel 625 at temperatures above 800 °C, while Nb and Ti oxides form above 1025 °C [24], suggesting that some oxygen was present in the system prior to densification of the part. Use of a reducing atmosphere or vacuum [17] throughout the entire sintering process is likely to reduce or eliminate this interparticle phase. Additionally, some XRD peaks in Fig. 5 indicate the presence of chromium carbide, previously reported to occur along the interparticle region as a result of Cr interaction with the binder [16]. Due to the binder burn-off step prior to sintering performed in this study, chromium carbide was present to a significantly smaller extent, with no clear visual indication of a chromium carbide phase in the cross-sectional images in Fig. 4. Since XRD is a large area characterization technique, it is likely that some localized regions were not fully

removed of binder and formation of chromium carbide still occurred. Binder residual can also lead to elevated levels of carbon in the system during sintering, which promote NbC formation.

3.2. Characterization of ESD coating

3.2.1. Effect of process parameters on surface condition

The improvement in surface condition with ESD of AA4043 is found to depend on the input energy. The lowest set of parameters results in an approximately 50 μm thick coating, however most of the interconnected network remains underneath (Fig. 6b). Increasing energy input results in a thicker coating, with the highest parameters (Fig. 6d) eliminating the near-surface porosity and achieving a coating density of 99.2 ± 0.3%.

During the ESD process, localized melting occurs on both the surface of the BJAM part and the consumable electrode. Formation of the aluminide coating is expected to occur as the AA4043 deposition mixes with the melted Inconel 625 substrate, depicted in the process schematic in Fig. 7a–c. The quantity of localized melting on the electrode and base metal is a function of the energy input, with higher energy shown to enhance mass transfer to the substrate at ESD frequencies under 1 kHz [25]. This can explain the reduction in the outer porous region shown in Fig. 6 with increasing input energy. A small energy input results in superficial melting, leaving a porous region underneath the dense coating. A higher energy input results in greater melting, vaporization and ejection of material, which contributes to the elimination of the interconnected pores. A second mechanism for densification is observed by the partially melted Inconel 625 powders near the bottom of the coating. A small amount of infiltration occurs, in which the molten Ni-Al mixture flows into open pores (Fig. 7d,e). The depth of infiltration observed was limited to 70 μm due to the rapid solidification of the molten mixture.

Visual analysis of coated BJAM parts reveals that surface roughness is influenced by the deposition energy, with more uneven buildup and material splashing visible at higher deposition energy Fig. 8b. All surfaces demonstrate the presence of scattered aluminum oxide particles while displaying slight non-uniformity in the Al, Cr, Si and Ni distributions (shown in Fig. 8c).

Measured surface roughness values listed in Table IV match the visual observations. All coatings exhibit a lower arithmetic mean height (R_a) than the uncoated surface, with low energy input resulting in the lowest R_a and the lowest peak to valley distance (R_z). However, high energy input results in higher R_z values than an uncoated sample, suggesting that high energy coatings have localized regions with significant buildup. Greater surface texture has the negative consequence of increasing oxidation mass gain by increasing the exposed surface area. This problem has been identified in additively manufactured parts when evaluating oxidation kinetics [26] and becomes more of a problem in the sintered BJAM parts with extensive near-surface porosity. For the coated samples, the texture of high energy coatings results in a 6% surface area increase (R_{dr}) in comparison to a perfectly flat surface. This value is approximately 2% for low and medium energy coatings. Although the surface-visible texture of uncoated samples causes an approximate 7% surface area increase, this measurement does not consider the surface connected porosities inside the near-surface porous region that cannot be evaluated using an optical profiler. Therefore, post-processing with ESD significantly lowers the exposed surface area, in addition to providing good oxidation resistance [27,28] and hot corrosion protection [28–30] expected from nickel aluminides.

3.2.2. Coating composition

Initial depositions result in a Ni-rich aluminide, since the melted substrate is pure Inconel 625. Subsequent depositions cause melting of the previously formed aluminide layer, which is lower in Ni content. As a result, the aluminides forming near the top of the coating are Al-rich, whereas the near-substrate layers have higher Ni, Cr, Fe and Mo
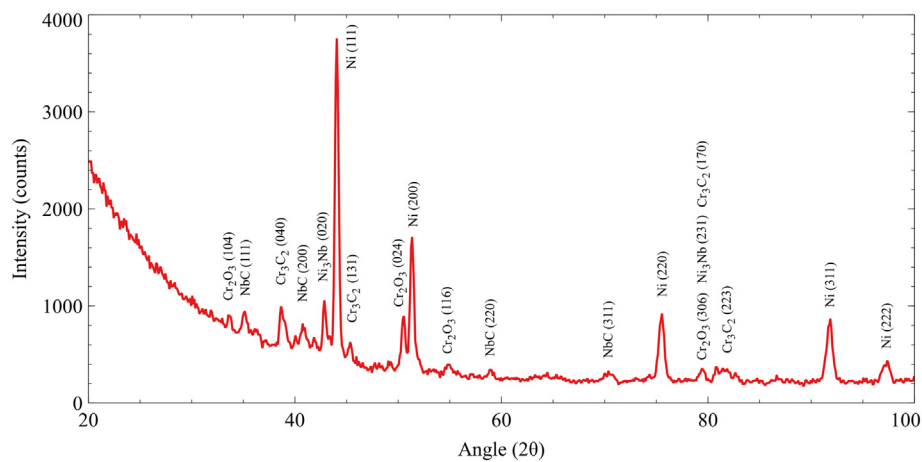
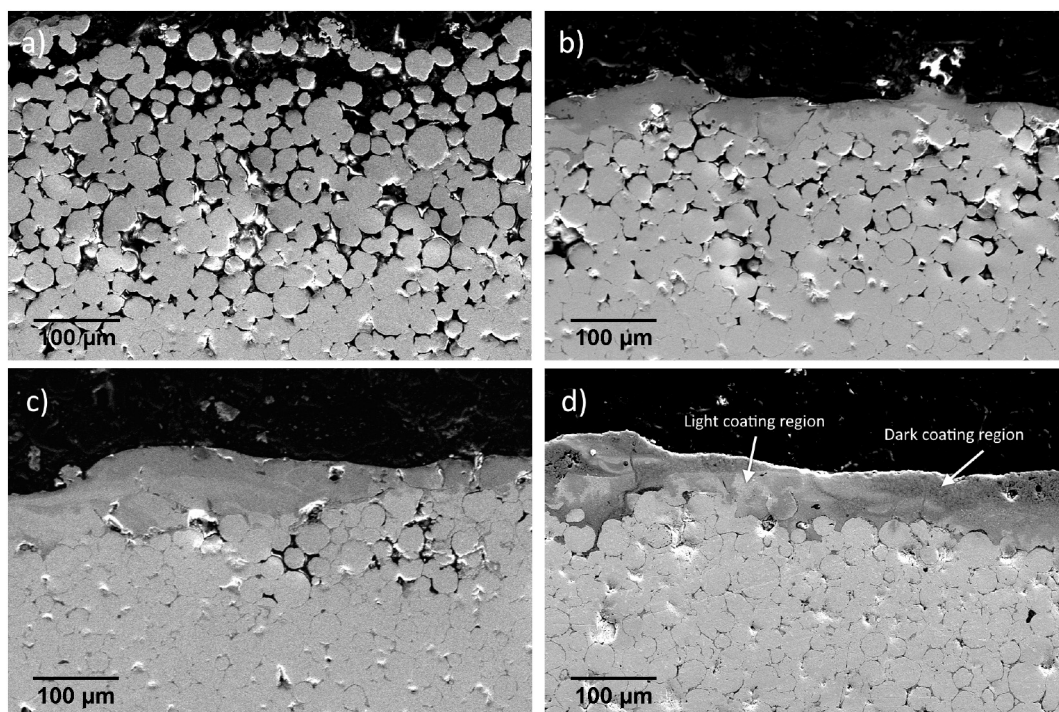**Fig. 5.** XRD analysis of a sintered BJAM Inconel 625 part.

Fig. 6. SEM surface image of Inconel 625 BJAM samples with a) no coating, b) low energy coating c) medium energy coating and d) high energy coating.

content. This concentration gradient can be seen in EDX line-scans of the coating, shown in Fig. 9b, with some variation due to non-uniformity in the mixing that occurs during deposition.

EDX analysis of the electrode after deposition confirms the presence of Ni and Cr elements associated with the Inconel 625 BJAM part (Fig. 9c,d), which were transferred to the electrode during the coating process and was previously reported to occur for a different electrode/substrate material pair [25]. Up to 100 μm of build-up occurs on the electrode surface, which further confirms that contact made between the electrode and the substrate during the ESD process results in mixing and bidirectional transfer of material.

GIXRD analysis of the coating is performed to confirm the presence of several nickel aluminide phases (Fig. 10). Due to the small penetration depth of GIXRD below 10 nm, the detected phases are those primarily near the top of the coating and are expected to be Al-rich. Nonetheless, Ni_3Al and NiAl peaks are still detected, in additional to Ni_2Al_3 and $NiAl_3$ peaks which are more likely to occur at that location.

3.2.3. Coating hardness

Microhardness measurements range significantly within the coating, correspond to the brightness differences seen in Fig. 6, and are summarized in Table V. The darker regions have higher hardness than the lighter regions typically found near the bottom of the coating, which are both harder than either the Inconel 625 base metal or AA4043 electrode. EDX analysis identifies the darker regions predominantly near the top of the coating as Al-rich whereas the lighter regions are Ni-rich. The nickel to aluminum ratio in these regions suggests that Ni_2Al_3 forms near the top of the coating, with NiAl and Ni_3Al forming nearer the base metal. According to the literature, Ni_2Al_3 has a noticeably higher hardness than other nickel aluminides (1142 HV), whereas the hardness of NiAl, Ni_3Al and even $NiAl_3$ is more difficult to distinguish (469–571 HV, 571–632 HV and 622–785 HV respectively) [31]. The extra alloying elements (Cr, Fe, Si) from the electrode and base metal are expected to change the hardness of the aluminide phases. The literature shows that Ni_3Al hardness values of 408 HV and Ni_2Al_3 hardness values of 969 HV are possible [31].
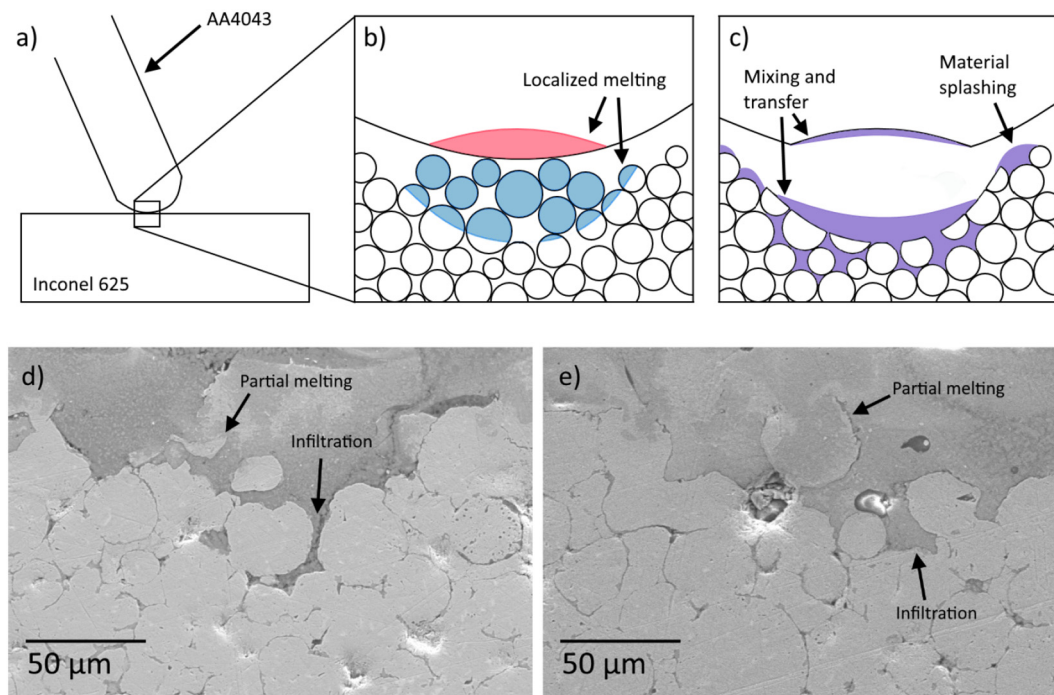
Fig. 7. Exaggerated schematic of ESD surface alloying process showing a) overview of electrode and substrate, b) capacitor discharge, and c) mixing of AA4043 and Inconel 625. SEM images d, e) show infiltration and partial melting as depicted in c).

3.3. Al and Ni diffusion during ESD

Numerous diffusion studies of Ni and Al systems have been performed in the literature due to the many practical applications of nickel aluminide coatings. Turbine blade coatings are selected to reduce hot corrosion and oxidation of the underlying Ni-superalloy material at elevated temperatures, while having the required strength and ductility to withstand the mechanical and thermal stresses experienced during operation. A majority of coatings are formed by diffusion techniques, including pack calorizing, slurry aluminizing, chemical vapor deposition and electric arc vacuum deposition [31–33]. An Al containing precursor or powder – sometimes alloyed with Cr, Si and/or Y – interacts with the superalloy surface and forms an aluminide intermetallic. In the case of Ni-superalloy components, nickel aluminides are formed as the deposited material diffuses into – or Ni diffuses out of –

Table IV
Surface roughness measurements for uncoated and coated samples.

Sample	R_a (µm)	R_z (µm)	R_{dr} (%)
Uncoated	25.9	263	7.1
Low energy	7.8	167	2.2
Medium energy	10.9	176	1.9
High energy	15.6	407	6.0

the turbine blade surface [31,32,34]. Exposure of the nickel aluminide to high temperatures in oxygen-rich environments results in the formation of protective aluminum oxide (Al_2O_3) scales that – along with secondary alloying elements in the coating – protect the underlying component from oxidation and hot corrosion.

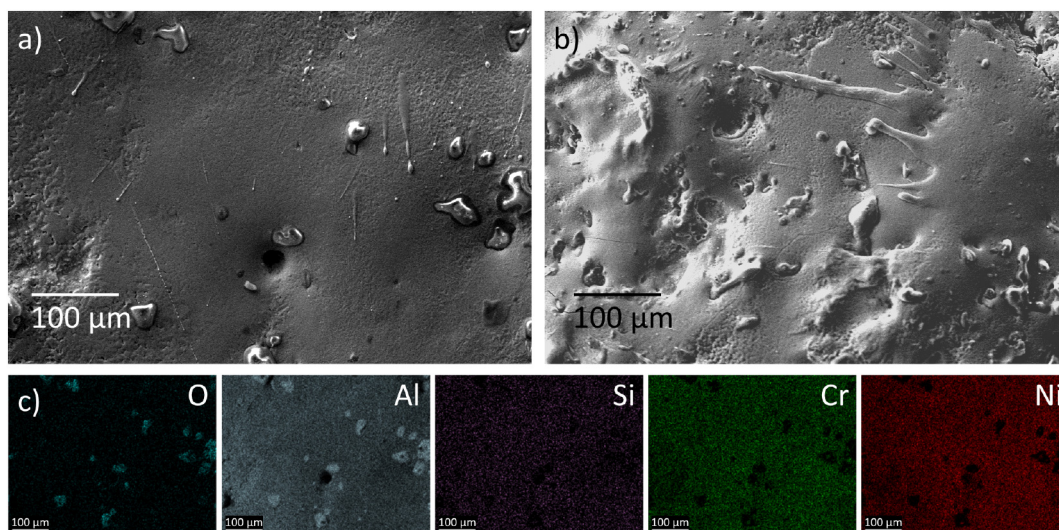The diffusivity and activation energies of Al and Ni atoms are highly

Fig. 8. SEM surface image of a) low energy coated sample, b) high energy coated sample, c) EDX scans of low energy coated sample surface.
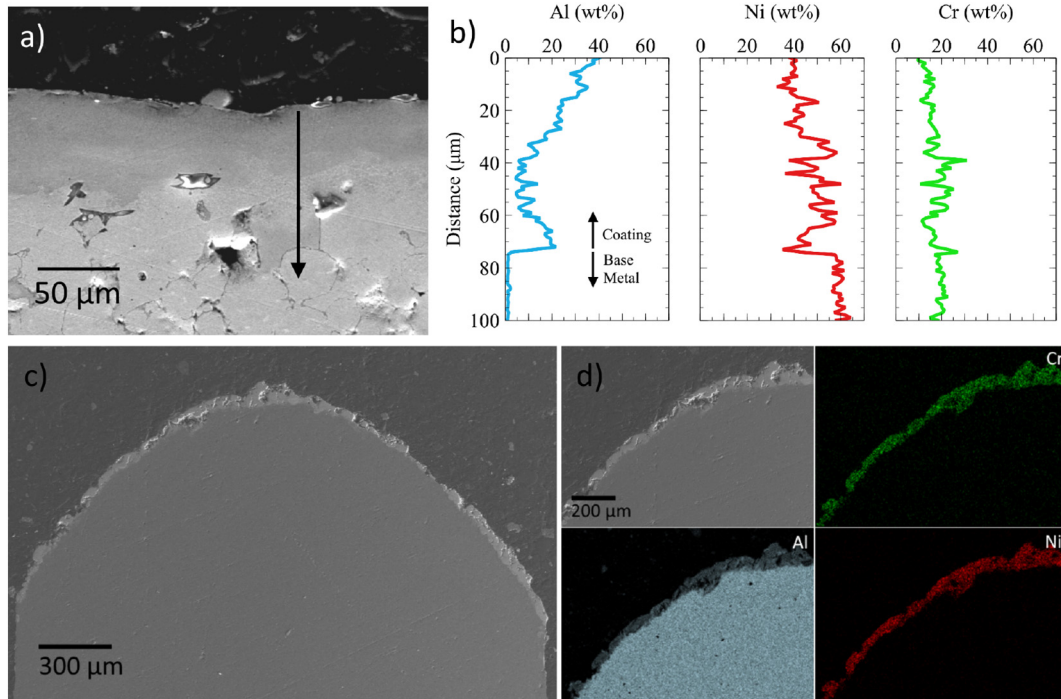
Fig. 9. SEM image of coating cross-sections depicting a) EDX line scan direction with b) EDX composition profile. Evidence of bidirectional material transfer is visible in c) SEM images and d) EDX maps of the cross-sectioned electrode.

dependent on the phase of the diffusing medium, the composition, and the temperature [35–37]. However, the initial conditions of nickel aluminide coatings created using ESD are different than those made with traditional diffusion techniques. Some techniques deposit an aluminum layer and then anneal the coating at temperatures above the melting point of aluminum but below the melting point of nickel [31], resulting in atomic diffusion across a liquid-solid Al-Ni interface. In an ESD process, material is deposited at high temperature and then cools rapidly, with physical mixing expected to occur when droplets from the electrode impact a molten substrate surface. This is in contrast to diffusion annealing processes that last several hours. To determine the role that diffusion plays in nickel aluminide formation when Al and Ni are both in a liquid state, an investigation into the extent of diffusion after the melted Inconel 625 substrate re-solidifies is required.

Under the assumption that no mixing occurs in the liquid-liquid Al-Ni state, the temperature profile of a molten 20 μm thick AA4043 droplet on a re-solidified 20 μm Inconel 625 layer as it cools after ESD is calculated using a one-dimensional heat diffusion equation,

Table V
Microhardness measurements with coating regions corresponding to Fig. 6d.

Location	$HV_{0.1}$
Inconel 625 substrate	109 ± 17
AA4043 electrode	46 ± 1
Dark coating region	962 ± 86
Light coating region	428 ± 44

$$\frac{\partial T}{\partial t} = \frac{k}{c_p \rho}\left(\frac{\partial^2 T}{\partial x^2}\right)$$

(2)

where T is the temperature (in kelvin), x is distance from the top of the droplet (in μm), t is the time (in seconds), and k, c_p, and ρ are the thermal conductivity, specific heat capacity and mass density of AA4043 (for $0 < x \le 20$) and Inconel 625 (for $20 \le x < 40$). The solution requires that a Neuman boundary condition ($\frac{\partial T}{\partial t} = 0$ at $x = 0$)
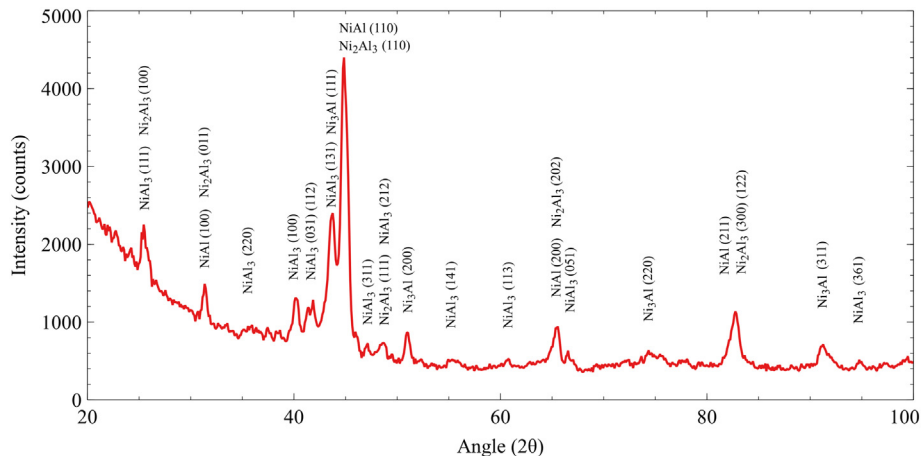

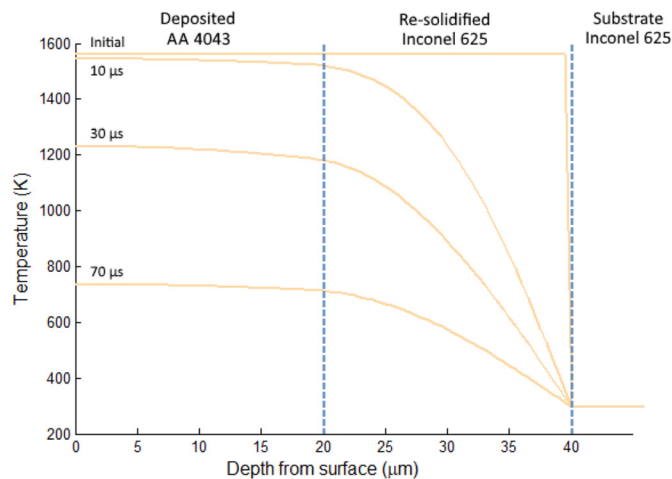**Fig. 10.** XRD analysis of AA4043 ESD coated BJAM Inconel 625 part.

Fig. 11. Temperature profile during cooling of AA4043 and re-solidified Inconel 625.

Table VI
Literature values of diffusion pre-exponential factor and activation energy for interdiffusion of Al and Ni.

Temperature (K)	D_0 (cm^2 s^{-1})	E_a (kJ K^{-1} mol^{-1})	Ref.
$722 \leq T < 919$	1.2E-9	90	[38]
$919 \leq T < 1269$	0.44	245	[38]
$1269 \leq T < 1623$	1.67	258	[39] as cited in [38]

and Dirichlet boundary condition ($T = 298.15$ at $x = 40$) be implemented, as well as an initial condition for the temperature of the molten alloys ($T = 1563.15$ at $t = 0$, which is the solidus temperature for Inconel 625). Eq. (2) is solved using ode45 (a built-in numerical ordinary differential equation solver) in MATLAB software package and the resulting temperature profile is shown in Fig. 11 for up to 70 μs of cooling.

The temperature at the deposited AA4043 and re-melted Inconel 625 boundary can now be used to determine the diffusion coefficient (D) as it changes over time, which is expected to follow an Arrhenius type relationship,

$$D = D_0 \exp\left(\frac{-E_a}{RT}\right) \tag{3}$$

where D_0 is a pre-exponential factor, E_a is the activation energy of species migration in the matrix, and R is the ideal gas constant ($8.31E - 3$ kJ K^{-1} mol^{-1}). The literature values of D_0 and E_a for interdiffusion of Al and Ni (Table VI) are used to determine the extent of diffusion during ESD, and it can be noted that diffusion occurs at an insignificant rate at the lowest temperature range.

Combining Eq. (3) with the Einstein relation (Eq. (4)) and temperature profile at the deposited AA4043 and re-solidified Inconel 625 interface, and then integrating the discretized diffusion distances from 0 μs to 70 μs (Eq. (5)) gives an approximation for the average total diffusion distance (d) that can be expected in ESD of AA4043 after the melted Inconel 625 substrate has re-solidified.

$$d = \sqrt{2Dt} \tag{4}$$

$$d = \int_0^{70} \sqrt{2D_0 \exp\left(-\frac{E_a}{RT}\right) \Delta t}\, dt = 3.6\ \mu m \tag{5}$$

As XRD analysis demonstrated in Fig. 10, the coating is primarily composed of nickel aluminides with the lack of peak at 38.4° suggesting a lack of pure aluminum. An average atomic diffusion of 3.6 μm between deposited AA4043 and re-solidified Inconel 625 during cooling cannot be solely credited for the formation of a fully nickel aluminide

coating free from unreacted Ni or Al. This suggests that the formation of the nickel aluminide is mostly attributed to the mixing and diffusion that occurs when both constituents are in the liquid state, which is not typically the case for most diffusion coatings. This also explains why the coatings have a combination of several different nickel aluminide phases; the rapid cooling time does not allow for enough diffusion to fully homogenize the coating.

4. Conclusion

Binder jet additive manufactured Inconel 625 parts form a near-surface porous region after sintering, which were post-processed using electrospark deposition (ESD).

- Higher energy input during the ESD post-processing is more effective at reducing the near-surface porosity. This is attributed to an increased melting in the porous substrate surface and increased material transfer during the ESD process.
- High energy input during ESD was correlated to a larger surface roughness, due to uneven material build-up and greater quantity of material transfer. However, all tested energy levels result in reduced surface roughness when compared to the uncoated BJAM parts.
- Bidirectional material transfer and mixing occurs during the ESD process. Elements from the electrode (Al, Si) and substrate (Ni, Cr, Fe) are found on the substrate and electrode, respectively.
- Deposition of an AA4043 material onto the Inconel 625 substrate forms a nickel aluminide intermetallic coating. Hardness measurements, EDX and XRD analysis indicate that several aluminide stoichiometries form. These include Ni_2Al_3, NiAl, $NiAl_3$, and Ni_3Al, which are formed along inverse Al and Ni concentration gradients through the coating. XRD analysis also confirms that no significant quantity of Al, transferred during the ESD post-processing, remains unreacted.
- A simplified diffusion model shows that the formation of the nickel aluminide is likely to occur at elevated temperatures above the melting point of both AA4043 and Inconel 625. The atomic diffusion that occurs after Inconel 625 solidifies is too limited to fully explain the lack of unreacted Al.

References

[1] SpaceX launches 3D-printed part to space, creates printed engine chamber, 4 (2014), http://www.spacex.com/news/2014/07/31/spacex-launches-3d-printed-part-space-creates-printed-engine-chamber-crewed , Accessed date: 22 June 2018.
[2] GE reports successful first test of Advanced Turboprop Engine, Met. Addit. Manuf. 56 (2018), http://www.metal-am.com/ge-reports-successful-first-test-advanced-turboprop-engine/ , Accessed date: 21 June 2018.
[3] Metal AM engine part completes maiden flight on Finnish fighter jet, Met. Addit. Manuf. 33 (2018), http://www.metal-am.com/metal-engine-part-completes-maiden-flight-finnish-fighter-jet/ , Accessed date: 21 June 2018.
[4] E. Sheydaeian, E. Toyserkani, A new approach for fabrication of titanium-titanium boride periodic composite via additive manufacturing and pressure-less sintering, Compos. Part B Eng. 138 (2018) 140–148, https://doi.org/10.1016/j.compositesb.2017.11.035.
[5] H. Fayazfar, M. Salarian, A. Rogalsky, D. Sarker, P. Russo, V. Paserin, E. Toyserkani, A critical review of powder-based additive manufacturing of ferrous alloys: process parameters, microstructure and mechanical properties, Mater. Des. 144 (2018) 98–128, https://doi.org/10.1016/j.matdes.2018.02.018.
[6] D. Greitemeier, C. Dalle Donne, F. Syassen, J. Eufinger, T. Melz, Effect of surface roughness on fatigue performance of additive manufactured Ti–6Al–4V, Mater. Sci. Technol. 32 (2016) 629–634, https://doi.org/10.1179/1743284715Y.0000000053.

[7] S. Leuders, M. Thöne, A. Riemer, T. Niendorf, T. Tröster, H.A. Richard, H.J. Maier, On the mechanical behaviour of titanium alloy TiAl6V4 manufactured by selective laser melting: fatigue resistance and crack growth performance, Int. J. Fatigue 48 (2013) 300–307, https://doi.org/10.1016/j.ijfatigue.2012.11.011.

[8] A. Mostafaei, S.H.V.R. Neelapu, C. Kisailus, L.M. Nath, T.D.B. Jacobs, M. Chmielus, Characterizing surface finish and fatigue behavior in binder-jet 3D-printed nickel-based superalloy 625, Addit. Manuf. 24 (2018) 200–209, https://doi.org/10.1016/j.addma.2018.09.012.

[9] E. Stevens, S. Schloder, E. Bono, D. Schmidt, M. Chmielus, Density variation in binder jetting 3D-printed and sintered Ti-6Al-4V, Addit. Manuf. 22 (2018) 746–752, https://doi.org/10.1016/j.addma.2018.06.017.

[10] H. Miyanaji, S. Zhang, L. Yang, A new physics-based model for equilibrium saturation determination in binder jetting additive manufacturing process, Int. J. Mach. Tools Manuf. 124 (2018) 1–11, https://doi.org/10.1016/j.ijmachtools.2017.09.001.

[11] T. Rasp, T. Kraft, H. Riedel, Discrete element study on the influence of initial coordination numbers on sintering behaviour, Scr. Mater. 69 (2013) 805–808, https://doi.org/10.1016/j.scriptamat.2013.09.003.

[12] J. Wang, H. Meng, H. Yu, Z. Fan, D. Sun, Wear characteristics of spheroidal graphite roll WC-8Co coating produced by electro-spark deposition, Rare Metals 29 (2010) 174–179, https://doi.org/10.1007/s12598-010-0030-6.

[13] X. Wei, Z. Chen, J. Zhong, L. Wang, Z. Hou, Y. Zhang, F. Tan, Facile preparation of nanocrystalline Fe 2 B coating by direct electro-spark deposition of coarse-grained Fe 2 B electrode material, J. Alloys Compd. 717 (2017) 31–40, https://doi.org/10.1016/j.jallcom.2017.05.081.

[14] K. Korkmaz, A.V. Ribalko, Effect of pulse shape and energy on the surface roughness and mass transfer in the electrospark coating process, Kovove Mater. 49 (2011) 265–270, https://doi.org/10.4149/km_2011_4_265.

[15] B.D. Sartwell, K.O. Legg, N. Price, D. Aylor, V. Champagne, M. Pepi, T. Pollard, Electrospark deposition for depot- and field-level component repair and replacement of hard chromium plating, Environ. Secur. Technol. Certif. Progr. 299 (2006), http://www.dtic.mil/docs/citations/ADA603502.

[16] P.D. Enrique, Y. Mahmoodkhani, E. Marzbanrad, E. Toyserkani, N.Y. Zhou, In situ formation of metal matrix composites using binder jet additive manufacturing (3D printing), Mater. Lett. 232 (2018) 179–182, https://doi.org/10.1016/j.matlet.2018.08.117.

[17] A. Mostafaei, E.L. Stevens, E.T. Hughes, S.D. Biery, C. Hilla, M. Chmielus, Powder bed binder jet printed alloy 625: densification, microstructure and mechanical properties, Mater. Des. 108 (2016) 126–135, https://doi.org/10.1016/j.matdes.2016.06.067.

[18] P. Nandwana, A.M. Elliott, D. Siddel, A. Merriman, W.H. Peter, S.S. Babu, Powder bed binder jet 3D printing of Inconel 718: densification, microstructural evolution and challenges, Curr. Opin. Solid State Mater. Sci. 21 (2017) 207–218, https://doi.org/10.1016/j.cossms.2016.12.002.

[19] S. Barella, A. Gruttadauria, C. Mapelli, D. Mombelli, P. Taiana, M. Bosatra, A. Morini, Solidification microstructure of centrifugally cast Inconel 625, China Foundry. 14 (2017) 304–312, https://doi.org/10.1007/s41230-017-7017-y.

[20] M.J. Cieslak, T.J. Headley, T. Kollie, A.D. Romig, A melting and solidification study of alloy 625, Metall. Trans. A 19 (A) (1988) 2319–2331, https://doi.org/10.1007/BF02645056.

[21] M. Sundararaman, P. Mukhopadhyay, S. Banerjee, Carbide precipitation in nickel

[22] base superalloys 718 and 625 and their effect on mechanical properties, TMS Superalloys 718 (1997) 625–706, https://doi.org/10.7449/1997/Superalloys_1997_367_378.

[23] L. Ferrer, B. Pieraggi, J.F. Uginet, Microstructural evolution during thermo-mechanical processing of alloy 625, Superalloys 718,625 Var. Deriv. 1991, pp. 217–228, , https://doi.org/10.7449/1991/Superalloys_1991_217_228.

[23] S. Floreen, G. Fuchs, W. Yang, The metallurgy of alloy 625, Superalloys (1994) 13–37, https://doi.org/10.7449/1994/Superalloys_1994_13_37.

[24] L. Kumar, R. Venkataramani, M. Sundararaman, P. Mukhopadhyay, S.P. Garg, Studies on the oxidation behavior of inconel 625 between 873 and 1523 K, Oxid. Met. 45 (1996) 221–244, https://doi.org/10.1007/BF01046827.

[25] X.R. Wang, Z.Q. Wang, T.S. Lin, P. He, Mass transfer trends of AlCoCrFeNi high-entropy alloy coatings on TC11 substrate via electrospark − computer numerical control deposition, J. Mater. Process. Technol. 241 (2017) 93–102, https://doi.org/10.1016/j.jmatprotec.2016.09.012.

[26] T. Sanviemvongsak, D. Monceau, B. Macquaire, High temperature oxidation of IN 718 manufactured by laser beam melting and electron beam melting: effect of surface topography, Corros. Sci. 141 (2018) 127–145, https://doi.org/10.1016/j.corsci.2018.07.005.

[27] S.O. Moussa, M.S. El-Shall, High-temperature characterization of reactively processed nanostructure nickel aluminide intermetallics, J. Alloys Compd. 440 (2007) 178–188, https://doi.org/10.1016/j.jallcom.2006.09.049.

[28] Z. Xu, J. Dai, J. Niu, L. He, R. Mu, Z. Wang, Isothermal oxidation and hot corrosion behaviors of diffusion aluminide coatings deposited by chemical vapor deposition, J. Alloys Compd. 637 (2015) 343–349, https://doi.org/10.1016/j.jallcom.2015.01.227.

[29] S.C. Deevi, V.K. Sikka, Nickel and iron aluminides: an overview on properties, processing, and applications, Intermetallics 4 (1996) 357–375, https://doi.org/10.1016/0966-9795(95)00056-9.

[30] G.W. Goward, Protective coatings – purpose, role, and design, Mater. Sci. Technol. 2 (1986) 194–200, https://doi.org/10.1179/mst.1986.2.3.194.

[31] Y. Tamarin, Protective Coatings for Turbine Blades, ASM International, 2002, https://books.google.com/books?id=LB9eItW_7CUC&pgis=1.

[32] S. Bose, High Temperature Coatings, Elsevier Butterworth-Heinemann, 2007.

[33] B. Bouchaud, B. Rannou, F. Pedraza, Slurry aluminizing mechanisms of Ni-based superalloys incorporating an electrosynthesized ceria diffusion barrier, Mater. Chem. Phys. 143 (2013) 416–424, https://doi.org/10.1016/j.matchemphys.2013.09.022.

[34] J.R. Davis, ASM Specialty Handbook: Heat-Resistant Materials, (1997), p. 591.

[35] M.M.P. Janssen, G.D. Rieck, Reaction diffusion and Kirkendall-effect in the nickel-aluminum system, Trans. Metall. Soc. AIME 239 (1967) 1372–1385.

[36] M.M.P. Janssen, Diffusion in the nickel-rich part of the Ni-Al system at 1000° to 1300 °C; Ni3Al layer growth, diffusion coefficients, and interface concentrations, Metall. Trans. A. 4 (1973) 1623–1633, https://doi.org/10.1007/BF02668017.

[37] A. Paul, The Kirkendall Effect in Solid State Diffusion, Eindhoven University of Technology, 2004.

[38] M. Hasaka, T. Morimura, Y. Uchiyama, S. ichiro Kondo, T. Watanabe, K. Hisatsune, T. Furuse, Diffusion of copper, aluminum and boron in nickel, Scr. Metall. Mater. 29 (1993) 959–962, https://doi.org/10.1016/0956-716X(93)90389-A.

[39] I.A. Akimova, V.M. Mironov, A.V. Pokoev, Aluminum diffusion in nickel, Izv. V. U. Z. Tsvetn. Met. (1985) 5.